Turbidity data obtained from image analysis in near critical hydrogen

Ana Oprisan [*]

Department of Physics and Astronomy, College of Charleston, 66 George Street, Charleston, South Carolina 29424, USA

Gurunath Gandikota and Denis Chatain

Université Grenoble Alpes and DSBT, IRIG, CEA, 38000 Grenoble, France

Yves Garrabos

ICMCB, UMR No. 5026, CNRS, Université de Bordeaux, and Bordeaux INP, 33600 Pessac, France

Daniel Beysens

Physique et Mécanique des Milieux Hétérogènes, CNRS, ESPCI, PSL Research University, and Sorbonne Université,
Sorbonne Paris Cité, Universités Paris 6 & Paris 7, 10 rue Vauquelin, 75005 Paris, France
and Université Grenoble Alpes and DSBT, IRIG, CEA, 38000 Grenoble, France

Video images are being used with increased frequency in science, supplanting current methods such as light scattering by statistical evaluation of the images. In this study we use light turbidity data due to density-induced refractive index fluctuations to obtain critical amplitudes from image analysis. In order to bring hydrogen (H_2) very close to its critical point, we place the sample cell under weightlessness using a magnetic levitation device. Images of an H_2-filled cell are taken near its critical temperature of 33 K by illuminating the cell with three different filters. We fit the turbidity data to a theoretical expression that allows us to estimate the critical amplitudes of isothermal compressibility and fluctuation correlation length. The values of isothermal compressibility and correlation length obtained from turbidity fitting are compared against literature values. Our data analysis shows a large sensitivity of the fitting parameters to the refractive index value and to even minute density deviations from criticality.

I. INTRODUCTION

We celebrate 150 years of critical phenomena studies that started with carbon dioxide liquefaction by Andrews. In his seminal work [1], Andrews introduced the concept of the critical point. It was van der Waals who introduced the principle of corresponding states, which asserts that the functional relations among pressure, temperature, and volume are the same for all fluids [2]. Among other optical techniques used for investigating critical phenomena, turbidity measures the amount of light transmitted through a fluid and helps probe the dynamics of density fluctuations near a fluid's critical point [3].

Close to the critical point, the physical properties of a fluid follow well-known universal laws [4–10]. When the critical point is approached, some parameters, such as the thermal expansion coefficient, isothermal compressibility, and thermal conductivity, diverge. Others, such as surface tension, liquid-vapor density difference, capillary length, and coefficient of thermal diffusivity, vanish. The fact that the above parameters asymptotically approach zero when approaching the critical point means that gravity effects become very large, which requires weightlessness for studying critical point phenomena. By heating or cooling a fluid, one can approach or move away from the liquid-vapor critical point. As a result, one can modify the properties of the liquid and vapor phases in a scaled way and thus study the liquid-vapor interface for a variety of fluid conditions.

Hydrogen (H_2) is a key player in space technology for propulsion and cooling [11,12]. Fluid management under the significant acceleration during takeoff and under microgravity in outer space poses significant technological challenges to space missions [13]. Among other difficulties, effective fluid management in microgravity requires a better understanding of thermo-hydrodynamics and phase change once buoyancy forces are canceled. Performing classical microgravity experiments with hydrogen is nearly impossible due to safety concerns [14], which leaves us with the alternative of counterbalancing gravity by using the diamagnetic property of H_2 [15].

We measured the turbidity dependence on temperature T for a fluid H_2 cell near its critical temperature T_c using three different optical filters, which allowed turbidity estimation at different wavelengths. In this study, we used the hydrogen levitation device (HYLDE) that allows gravity compensation by volumic magnetic forces induced by a magnetic field gradient (see [16,17] for an introduction to magnetic compensation of gravity and [14,15,18] and references therein for the mathematical derivation of effective gravity under magnetic compensation).

---
[*]oprisana@cofc.edu

Video images are increasingly used in many areas of science and technology as they allow a better understanding of physical processes than the more traditional light scattering methods. We show that image analysis of turbidity gives the same information on compressibility and correlation length of H_2 critical fluid as one gets with classical light scattering. By fitting the turbidity τ versus reduced temperature ($\epsilon = T/T_c - 1$) with well-established theoretical formulas [19–23] we found the values of two critical amplitudes: κ_{T0} for the isothermal compressibility and ξ_0 for the fluctuation correlation length.

Among the benefits of our approach, we mention that magnetic compensation of gravity allows a very close approach to critical temperature without gravity disturbances that usually affect critical fluids, e.g., buoyancy-driven instabilities and strong density gradients. The HYLDE cryogenics system uses a low-power, adjustable, light source to minimize the temperature disturbance of the probe. Another advantage of our approach is that we can visualize the whole sample, which allows us to detect density inhomogeneities. Working with three different filters centered on red, green, and blue wavelengths allows us to cross-check estimated values for susceptibilities based on turbidity measurements. Finally, we can use the same setup to study other critical phenomena, such as phase transition, and determine critical temperature with high precision (outside the scope of this study).

The present paper is organized as follows. First, we briefly review background information on both critical point scaling laws and turbidity. Next, the HYLDE setup is reviewed without repeating all the details of previous studies. Our results start with a critical review of existing data on H_2 critical parameters and the refractive index measurements near the critical point. The bulk of the section on results is concerned with extracting the critical amplitudes κ_{T0} and ξ_0 by fitting the turbidity τ versus reduced temperature ϵ graphs. We also compare our results against existing experimental data and theoretical predictions. Finally, we provide insight into the expected power law exponents predicted by the existing theoretical model of turbidity via numerical simulations.

II. BACKGROUND

A. Critical point phenomena

Near the liquid-vapor critical point, a number of thermodynamic quantities diverge asymptotically as power laws when temperature is varied [4,5,9,24]. Among others, the isothermal compressibility κ_T and the correlation length of density fluctuations ξ both diverge as power laws near the critical temperature T_c. For example, the susceptibility χ and the fluctuation correlation length ξ are written as [4]

$$\chi = p_c \kappa_T = \Gamma_0 \epsilon^{-\gamma}(1 + a_\chi \epsilon^\Delta + \cdots),$$
$$\xi = \xi_0 \epsilon^{-\nu}(1 + a_\xi \epsilon^\Delta + \cdots). \quad (1)$$

Here p_c is the critical pressure and $\epsilon = \frac{T}{T_c} - 1$ is the reduced temperature, with T and T_c the temperature and critical temperature, respectively. In addition, $\Gamma_0 = p_c \kappa_{T0}$ and ξ_0 are critical amplitudes that depend on the considered fluid;

$\gamma = 1.24$ and $\nu = 0.63$ are universal critical exponents. The existence of universal relations, the so-called scaling laws, between exponents means that only two critical exponents are independent. Consequently, all the amplitudes are connected by universal ratios and only two critical amplitudes are independent [8–10,25]. Therefore, the experimental estimation of the amplitudes, such as Γ_0 and ξ_0 from Eq. (1), is of prime importance for the validation of the two-scale-factor universality for simple fluids that are expected to belong to the three-dimensional Ising-like systems [8,10,25]. In Eq. (1) we also note that the terms inside the parentheses correspond to nonanalytical corrections characterized by the universal value $\Delta = 0.50$ of the corresponding exponent [26,27]. The amplitudes of the nonanalytical correction such as a_χ or a_ξ are fluid dependent and only one among these nonanalytic amplitudes can be used to characterize each fluid (see, for example, [28]). Typically, their magnitudes are of the order of unity. Since in this study the temperature remains close to T_c, the small contributions of nonanalytical amplitudes are not taken into account hereafter. As a result, we are only concerned with the estimation of critical amplitudes Γ_0 and ξ_0 from turbidity observed in recorded video images of a critical H_2 cell.

B. Turbidity

Turbidity is obtained from measured light transmission $\mathcal{T}$ through a sample with thickness e [19–21],

$$\mathcal{T} = I_T/I_0, \quad (2)$$

where I_T is the transmitted light intensity and I_0 is the incident light intensity. Turbidity can be calculated as

$$\tau = -\frac{1}{e}\ln(\mathcal{T}). \quad (3)$$

Very close to critical point, turbidity is only due to the Rayleigh scattering of light [19]. The enhancement of refractive index fluctuations due to the density (order parameter) fluctuations becomes increasingly important as one approaches the critical point and leads to the so-called critical opalescence phenomenon [4–6,9]. According to the Ornstein-Zernike theory, turbidity is related to the scattered light intensity integrated over all scattered angles [22,23]

$$I(k) = AT\kappa_T \sin^2(\Phi)/[1 + (q\xi)^2], \quad (4)$$

where q represents the amplitude of the transfer wave vector between the incident wave vector k_i and scattered k_s, i.e., $q = |k_i - k_s| = 2k_0 \sin(\theta/2)$. The wave vector of the incident light is $k_0 = 2\pi n/\lambda_0$, Φ is the angle between the polarization of the incident beam wave vector and the scattered light wave vector, n is the refractive index of the fluid, λ_0 is the wavelength of the incident light in the vacuum, and θ is the scattering angle. The factor A is given by [19–21]

$$A = \frac{\pi^2}{\lambda_0^4}\left(\rho\frac{\partial n^2}{\partial\rho}\right)_T^2 k_B = \frac{\pi^2}{\lambda_0^4}\left(\frac{(n^2-1)(n^2+2)}{3}\right)^2 k_B, \quad (5)$$

where k_B is the Boltzmann constant. The factor A varies strongly with both λ_0 (due to the λ_0^{-4} factor) and with the

index of refraction n. The index of refraction n corresponds to λ_0 at $T = T_c$ and $\rho = \rho_c$. For the derivative $\frac{\partial n^2}{\partial \rho}$, we used Lorentz-Lorenz relationship

$$\frac{1}{\rho} \frac{n^2 - 1}{n^2 + 2} = r(\lambda), \tag{6}$$

where $r(\lambda)$ is almost constant at a given wavelength.

It should be noticed that varying the wavelength from blue (0.45 μm) to red (0.65 μm) has the same effect on turbidity as varying the sample's thickness by a factor

$$\frac{e_1}{e_2} = \frac{\ln(\lambda_1)}{\ln(\lambda_2)} \approx 2. \tag{7}$$

Indeed, consider two samples of thicknesses e_1 and e_2, illuminated by light with wavelengths λ_1 and λ_2, respectively. From Eq. (3) and the definition of the factor A in Eq. (5) one gets, for the ratio of turbidities of the two samples,

$$\frac{\tau_2}{\tau_1} = \frac{e_1}{e_2} \frac{\ln(\lambda_2)}{\ln(\lambda_1)},$$

which leads to Eq. (7) for $\tau_1 = \tau_2$.

Integrating Eq. (4) over all scattering angles, one gets the turbidity [19–21]

$$\tau = A\pi T_c(1 + \epsilon)\kappa_T F(a) + \tau_B. \tag{8}$$

The parameter τ_B is a background contribution due to the light attenuation other than scattering by critical fluctuations, e.g., Brillouin and Raman scattering and light reflection or absorption by the windows. The background turbidity τ_B also includes the effect of uncertainty in the estimation of I_0. The function $F(a)$ is given by [19–21]

$$F(a) = \left(\frac{2a^2 + 2a + 1}{a^3}\right) \ln(1 + 2a) - 2\left(\frac{1 + a}{a^2}\right) \tag{9}$$

and represents an interference term which depends on $a = 2(k_0\xi)^2$ and whose limit value for $\epsilon \to \infty$ is 8/3 [29]. For a reasonable range of 1 Å $\leqslant \xi_0 \leqslant$ 3 Å and all wavelengths in the visible spectrum, the interference function $F(a)$ in Eq. (9) is at least at 77.7% of its limit value of 8/3 for all $\epsilon > 10^{-3}$. In other words, for $\epsilon > 10^{-3}$ the interference function is quasiconstant and its effect on turbidity formula given by Eq. (8) can be neglected. This approximation corresponds in H_2 to an off-critical temperature of about $T - T_c > 33$ mK (see the discussions on Fig. 5 in Sec. IV C below regarding the asymptotic behavior of turbidity for both large and very small values of reduced temperature).

III. EXPERIMENTS AND METHODS

A. Magnetic levitation setup

Due to earth's gravity, fluids near the critical point compress under their own weight. Additionally, due to the divergence of the thermal expansion coefficient near the critical point, minute temperature gradients induce strong convective flows inside critical fluids [4–7,9,10,30]. In order to compensate for these strong gravity effects, we carried out the experiments using the HYLDE cryogenic facility [14–16]. The

HYLDE setup uses a magnetic field up to 10 T generated by a cylindrical superconducting coil. Hydrogen is diamagnetic; thus it can levitate near the upper end of the coil where a nearly constant magnetogravitational potential field is produced. Gravitational field compensation is possible because a diamagnetic substance, such as H_2, placed in a magnetic field is subject to a force that is proportional to its magnetic susceptibility and to the local gradient $(\vec{B} \cdot \vec{\nabla})\vec{B}$ [see Eq. (1) in [14] and Eq. (1) in [16]]. The theoretical background for magnetic compensation of gravity in H_2 is detailed in [16]. With respect to the experimental setup, without repeating the very detailed description and schematics presented in [16], we only mention that the apparatus consists of a cryostat that contains the superconducting coil and an anticryostat containing the sample and the optics [see Fig. 1 in [16], Fig. 3(a) in [18], and Fig. 1(a) in [14] for details]. The Nb-Ti superconducting coil inside the cryostat is dipped in liquid helium at a temperature of 2.16 K and a pressure of 0.1 MPa. The experimental cell is mounted inside the anticryostat and maintained under a vacuum of less than 10^{-7} mbar. Endoscopes for a light source and a video camera are mounted inside the anticryostat. The positions of the endoscopes can be adjusted independently. A more detailed schematics of HYLDE is shown in Fig. 1(a) of [31] or [14] together with an actual photo of the experimental cell of size $7 \times 7 \times 7$ mm^3 [see Fig. 1(b) in [31] or [14]]. The same HYLDE setup was used in [32] (see their Fig. 10) with a $3 \times 3 \times 3$ mm^3 cell.

It has been demonstrated [17] that the magnetic levitation technique using a solenoid of cylindrical configuration only achieves total compensation of gravity at a single point in space. As a result, there is always a residual gravitational field radially directed towards the center of the cell. The uniformity of the gravitational field depends on the size of the cell (see the in-depth analysis of the effective gravity homogeneity inside cylindrical samples under magnetic levitation in [16]). Using the HYLDE setup, a uniform magnetogravitational potential field better than 1% and 2.5% can be achieved in cells of side $h = 3$ and 7 mm, respectively [16].

Hydrogen can be found in two states of spin polarization: ortho and para. When H_2 is cooled down, the balance between ortho-H_2 (o-H_2) and para-H_2 (p-H_2) is shifted and the percentage of p-H_2 (antiparallel spins) increases from about 33% at room temperature to 96% at 30 K (see [33]). As the temperature decreases towards T_c, more o-H_2 (parallel spins of H nuclei) transforms into p-H_2, which in turn determines a decrease of T_c itself. In our experiment, the change in temperature was much faster than the slow drift of T_c because of o-H_2 to p-H_2 conversion. It has been found that T_c follows an exponential relaxation with a time constant of about 2500 min [34]. As the experiments are performed within hours after filling the cell with the fluid initially at room temperature, the H_2 state is thus normal-H_2 (n-H_2). Its critical point is defined by a range of values for T_c, p_c, and ρ_c given in Tables I and II.

Hydrogen is filled inside the cell by using a capillary tube of inner diameter 0.5 mm. The capillary tube is fitted with a thermal switch made of a small block of copper continuously cooled under the triple point of H_2 by a copper wire connected to the helium bath of the cryostat. The switch is heated using a resistive heater. In the absence of heating, the H_2 inside

TABLE I. Relevant critical parameters for n-H_2 based on our extensive review of the existing literature.

T_c (K)	p_c	ρ_c	Polarizability (cm^3/mol)	Ref.
33.18	9864.8 mmHg	29.87 kg/m^3		[35]
		29.88 kg/m^3	2.0372	[36]
33.19	9864.8 mmHg	30.12 kg/m^3		[37]
33.19	9865 mmHg	14.94×10^{-3} mol/cm^3		[38]
33.19	1.315 MPa = 12.98 atm	30.12 kg/m^3 = 14.94 mol/l	2.0372	[39]
33.18	12.98 atm	30.12 kg/m^3 = 0.01494 mol/cm^3 l	2.0372	[40]
			2.0373	[41]

the capillary tube freezes, thus closing the cell. To fill or empty the cell, the switch is heated up, thus melting solid H_2 inside the capillary tube. To determine the critical density, the cell is filled up to half its height at a temperature to within 50 mK of T_c and the meniscus is monitored under $g = 1$ while temperature slowly increases from $T_c - 50$ mK towards T_c. If the level of the meniscus does not change within the optical resolution while changing the temperature, it means that the cell is filled at its critical density (see also [34] for a detailed description of the procedure). A measuring accuracy of 0.2 mm for the meniscus corresponds to a density uncertainty of $(\rho - \rho_c)/\rho_c \approx 2\%$. The experimental cell is provided with thermal bridges, strands of copper wires connecting the bottom flange of the anticryostat, which is maintained at liquid helium temperature. Resistive heaters in thermal contact with the cell are used for both heating and controlling the temperature of the cell. The temperature is monitored by two thermometers attached on the cell's wall. The temperature control of the cell achieved with a standard proportional-integral-derivative control system is better than 0.3 mK.

B. Turbidity measurement method

Traditionally, light transmission is measured with a thin (0.1 mm) polarized laser beam. Here light transmission is measured by a fixed gain camera on the image itself, pixel by pixel or averaged over a window (Fig. 1). In order to avoid collecting multiple scattered light, the total aperture angle of the collecting lens is small ($\alpha = \pm0.75°$ or $\alpha = 13$ mrad), similar to laser transmission methods. This small aperture is the result of a long depth (0.4 m typically) of focus. The CCD camera resolution was 1024×1024 pixels at 30 frames/s [34], although because of the small aperture of the optical

system only about 750×750 pixels were used. Incident light is produced by a collimated beam originating from a white-light lamp with switchable interferential filters centered on blue (465.2 nm, bandwidth 71 nm), green (519.4 nm, bandwidth 92 nm), and red (669.4 nm, bandwidth 78 nm).

A detailed view of the cell is shown in Fig. 2 (see also Fig. 2 in [34] for more details on the optical parameters of the HYLDE). The cell is cylindrical with a sapphire window at one end and a mirror at the other end [see Fig. 2(a)]. Its thickness is $e_0 = 21.00$ mm and its radius is 20 mm. The mirror placed at the end of the cell reflects the light back, which makes the final light path through the fluid $e = 2e_0$. Compared to a laser beam, which typically heats up the fluid by 1 mK/mW, this method has the advantage of dissipating less power.

We used an eight-bit CCD camera, which allowed for 256 gray-level discretization of recorded images. In gray levels, the maximum intensity is 255 [see Figs. 3(a) and 3(b)] and the minimum we recorded is about 6 [see Figs. 3(c) and 3(d)], which corresponds to the electronic noise of the camera. As a result, the minimum detectable transmission with our setup is $\mathscr{T}_{min} \approx 6/255 \approx 0.0235$, which corresponds to a maximum turbidity $\tau_{max} = (-1/e)\ln(\mathscr{T}_{max}) \approx 100$ m^{-1}. Accordingly, the maximum transmission is $\mathscr{T} \approx (255 - 6)/255 \approx 0.976$, which corresponds to a minimum turbidity value of $\tau_{min} = (-1/e)\ln(\mathscr{T}_{min}) \approx 0.6$ m^{-1}. In Fig. 3 we show two representative images of the cell far from the critical point [see Figs. 3(a) and 3(b)] and closer to T_c [see Figs. 3(c) and 3(d)]. The histograms of gray-level intensities [Figs. 3(c) and 3(d)] correspond to the squares marked and placed at the same location in the corresponding images [Figs. 3(a) and 3(b)]. As the temperature approaches T_c, the histogram becomes narrower, i.e., towards more homogeneous illumination, and shifts to lower light intensities.

TABLE II. Relevant critical parameters for p-H_2 based on our extensive review of the existing literature.

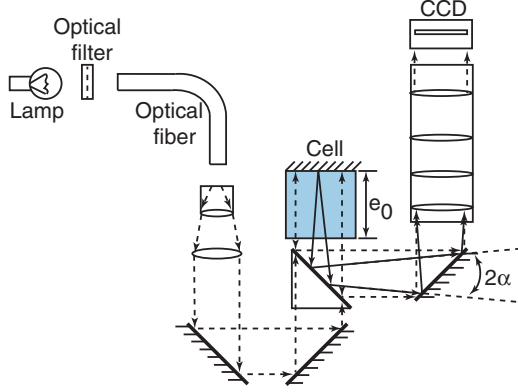| T_c (K)	p_c	ρ_c	Polarizability	Ref.
32.976	9696.84 mmHg	31.43 kg/m^3		[37]
32.938	1.28377 MPa	15.556 mol/dm^3		[41]
32.976	9696.8 mmHg	0.015 59 mol/cm^3		[35]
32.933		0.03136 g/cm^3		[42]
32.994	12.770 atm	1/62.8 mol/cm^3		[43]
32.976	1.2928 MPa = 12.759 atm	31.43 kg/m^3 = 15.59 mol/l	2.0279 cm^3/mol	[39]
32.976	12.759 atm	0.015 59 mol/cm^3	2.0279 cm^3/mol	[40]
			1. 004 cm^3/g	[36]

FIG. 1. Schematic representation of the HYLDE optical setup. The total angular aperture is $2\alpha = 26$ mrad. The solid arrows indicate the 2α aperture.

IV. RESULTS

A. Critical review of the literature on critical parameters for hydrogen

The turbidity given by Eq. (8) is sensitive to selected values for n and λ_0. To assess its sensitivity, we performed a first-order (linear) perturbation of the logarithm of Eq. (8) and found

$$\frac{\delta\tau}{\tau} = \left(\frac{1}{A}\frac{\partial A}{\partial n} + \frac{1}{F(a)}\frac{dF(a)}{da}\frac{\partial a}{\partial n} \right)\delta n$$

$$+ \left(\frac{1}{A}\frac{\partial A}{\partial \lambda} + \frac{1}{F(a)}\frac{dF(a)}{da}\frac{\partial a}{\partial \lambda} \right)\delta\lambda. \quad (10)$$

The refractive index sensitivity is dominated by the first term $\frac{1}{A}\frac{\partial A}{\partial n} = \frac{4n(1+2n^2)}{(n^2-1)(n^2+2)}$. For $n = 1.05$ this term $\frac{1}{A}\frac{\partial A}{\partial n} \approx 40$ and for $n = 1.04$ the same term is $\frac{1}{A}\frac{\partial A}{\partial n} \approx 50$. The first factor
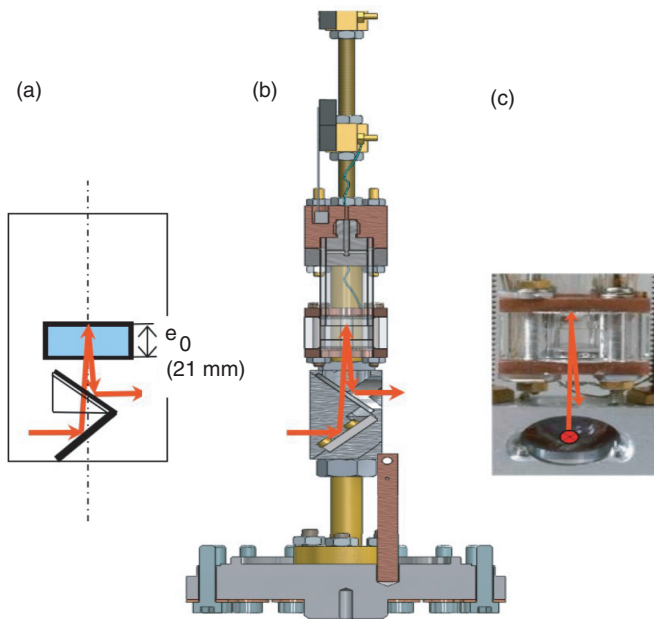

FIG. 2. Hydrogen sample cell and optical paths of $e = 2e_0 = 2 \times 21$ mm in the fluid. (a) Schematics. (b) Details. (c) Photo.
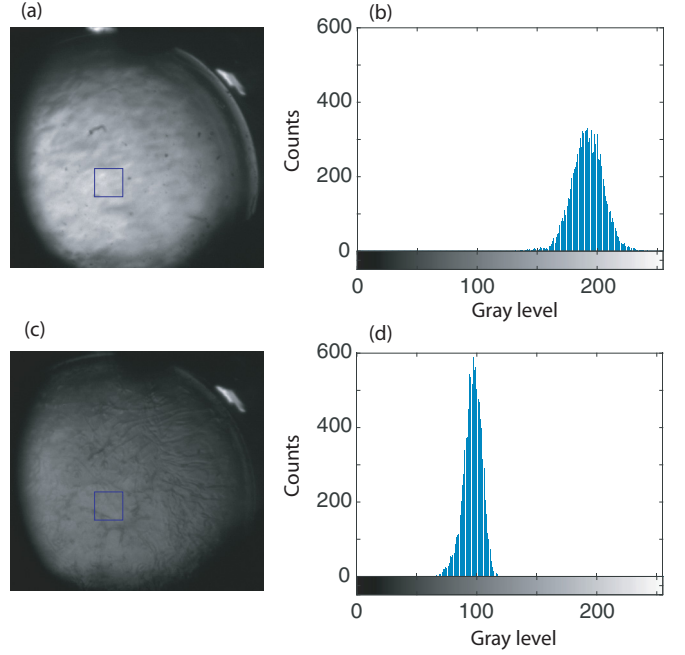

FIG. 3. Images of (a) and (c) the sample cell and (b) and (d) the corresponding gray-level histograms of the region of interest. Far from the critical point of H_2, $T - T_c = 993.5$ mK, (a) the image is bright and (b) the gray-level distribution shifts towards lighter levels. Closer to critical point $T - T_c = 2$ mK, (c) there is less transmitted light and (d) the corresponding histogram shifts towards darker gray levels.

in the second term of δn is $\frac{1}{F(a)}\frac{dF(a)}{da} \to 1$ and the second factor $\frac{\partial a}{\partial n} \to 0$ as $T \to T_c$. Similarly, wavelength sensitivity is dominated by the first term $\frac{1}{A}\frac{\partial A}{\partial \lambda} = \frac{4}{\lambda}$, whereas the second term vanishes as $T \to T_c$. Therefore, the dominant terms, in absolute value, that drive the relative error of turbidity are

$$\frac{\delta\tau}{\tau} = \frac{4n^2(1+2n^2)}{(n^2-1)(n^2+2)}\frac{\delta n}{n} + 4\frac{\delta\lambda}{\lambda}. \quad (11)$$

Of the two terms above, the relative error on the refractive index $\delta n/n$ has a factor that is one order of magnitude larger than the wavelength uncertainty $\delta\lambda/\lambda$. This justifies our in-depth review of the literature while searching for accurate refractive indices near T_c.

We thoroughly reviewed the literature for available data regarding $n\text{-}H_2$ (see Table I) and $p\text{-}H_2$ (see Table II). Our experiment was performed shortly after the H_2 reached the critical temperature such that the liquid likely did not reach ortho-para equilibrium and $n\text{-}H_2$ dominates in our experiment.

B. Index of refraction

The refractive index n has been derived in two different ways: (i) from the Lorentz-Lorenz formula of specific refraction

$$r = (n^2 - 1)/(n^2 + 2)/\rho \quad (12)$$

or (ii) from the Clausius-Mossotti relation

$$\mathscr{R}_{CM} = (\phi - 1)/(\phi + 2)/\rho, \quad (13)$$

TABLE III. Refraction index n_c near critical temperature. The wavelengths in our experiment were 669.4 nm (red), 519.4 nm (green), and 465.2 nm (blue).

n-H$_2$				p-H$_2$				
n_c	Red	Green	Blue	n_c	Red	Green	Blue	Source
1.04911 (546.2 nm)				1.04667–1.04706				[38,44]
	1.04857	1.04929	1.04977		1.04613–1.04652	1.04685–1.04724	1.04733–1.04772	[38,44] & Eq. (15)
1.04726				1.04489–1.04527				[44]
	1.04857	1.04929	1.04977		1.04613–1.04652	1.04685–1.04724	1.04733–1.04772	[44] & Eq. (13)
				1.04544–1.04582				[41]
					1.04624–1.04663	1.04679–1.04718	1.04713–1.04753	[41] & Eq. (13)
				1.050958				[42]

where $\phi = n_\infty^2$ is the dielectric constant and n_∞ is the refractive index for infinite wavelength. The value of $\mathscr{R}_{CM}$ can be experimentally determined from the polarizability using $\mathscr{R}_{CM} = P/M$, where M is the molecular weight and P is the molar polarizability. Once determined, the value of $\mathscr{R}_{CM}$ is then used to estimate the dielectric constant ϕ and the corresponding refractive index n_∞. To avoid notation confusion, we use ϕ for the dielectric constant throughout the paper and reserve ϵ only for the reduced temperature.

While reviewing the literature on the refractive index measurements near the critical point, we found two sets of data: (a) the index of refraction is given at a particular wavelength, or set of wavelengths, and (b) the wavelength is not specified (see Table III). The second case occurs because the Clausius-Mossotti relationship (13) was used to determine the refractive index n_∞ from the dielectric constant. In both cases, we computed wavelength corrections for the refractive index based on Cauchy's formula of specific refraction [45]

$$r(\lambda) = r_\infty + A/\lambda^2 + B/\lambda^4, \quad (14)$$

with $A = 0.779\,956\,9 \times 10^6$ and $B = 0.495\,126 \times 10^{12}$ for λ in angstroms and r in cm^3/g. However, if the specific refraction is in mol/dm^3 as in [41], then Cauchy's coefficients must be multiplied by the molar mass/1000.

Based on Eq. (12), the refractive index is calculated with

$$n(\lambda) = \sqrt{\frac{1 + 2\rho r(\lambda)}{1 - \rho r(\lambda)}}. \quad (15)$$

Sometimes the specific refraction or the refraction index was measured using interferometry methods at a given wavelength. In such cases, when the wavelength λ_1 is known, to avoid uncertainties regarding r_∞, we computed the refractive index at the wavelengths in our experiment $n(\lambda_2)$ based on a known value of the refractive index $n(\lambda_1)$. Based on Eqs. (12) and (14) one gets

$$\frac{n_1^2 - 1}{n_1^2 + 2}\frac{1}{\rho} = r_\infty + A/\lambda_1^2 + B/\lambda_1^4 \quad (16)$$

at a given wavelength λ_1. By rewriting the same relationship at a different wavelength λ_2 and eliminating r_∞ one gets

$$n(\lambda_2) = \sqrt{\frac{n(\lambda_1)^2 + 2\beta}{1 - \beta}}, \quad (17)$$

with $\beta = \rho\frac{n(\lambda_1)^2+2}{3}(\frac{1}{\lambda_2^2} - \frac{1}{\lambda_1^2})[A + B(\frac{1}{\lambda_2^2} + \frac{1}{\lambda_1^2})]$. Equation (17) has been used to handle the calculation of wavelength-dependent refractive indices when the refractive index is known at a specific wavelength λ_1 (see rows 1 and 2 in Table III).

1. Refractive index values at T_c (Table III)

Souers derived a simple equation for all liquid and gases from 30 to 100 K [38,44],

$$n(546.2 \text{ nm}) = 1 + 3.15 \times 10^{-6}\rho, \quad (18)$$

where the density ρ is in mol/m^3, with molar weight of H$_2$ equal to 2.015 94 g/mol. It has been stated that the above equation "is a reasonable estimating procedure for all hydrogen isotopes in all phases. It will probably be accurate to a few percent" [44]. A crude estimate of the index of refraction with the above formula at T_c gives (see the first row of Table III) $n_c = 1.046\,67 - 1.047\,06$ for p-H$_2$ and $n_c = 1.049\,11$ for n-H$_2$. Since we know the wavelength λ_1 for which the empirical formula (18) is valid, we used Cauchy's dispersion formula [45] (see the second rown in Table III) to correct the index of refraction value for our filters according to Eq. (17).

Stewart [44] derived a specific refraction formula from measurements of the dielectric constant. Stewart's formula is for p-H$_2$ and is limited to temperatures below 100 K and densities below 0.080 g/cm^3. The density dependence of specific refraction (see p. 13 in [45]) is

$$r_\infty = 1/\mathscr{P} = 0.995\,75 - 0.090\,69\rho + 1.1227\rho^2, \quad (19)$$

where polarizability $\mathscr{P}$ is in cm^3/g and ρ in g/cm^3. With r_∞ from Eq. (19) we estimated the refractive index using Eq. (12) to be $1.044\,89 \leqslant n_c \leqslant 1.045\,27$ for p-H$_2$ with densities in the range 29.87 kg/m^3 $\leqslant \rho_c \leqslant 30.12$ kg/m^3, and $n_c = 1.047\,26$ for n-H$_2$ with $\rho_c = 31.43$ kg/m^3. We also used Eq. (14) to account for Cauchy's correction (see row 4 in Table III).

Koch [46] determined the refractive index at 20 wavelengths from 230.2 to 546.1 nm. Kirn [47] determined the refractive index at 15 wavelengths from 185.4 to 546.1 nm [45]. "The average deviation from those experimental points of Koch and Kirn lying in the visible region is 0.04%" [45]. Their formula is given by Eq. (19).

McCarty *et al.* [40] (see pp. 1–31 therein) arrived at a formula similar to Eq. (19),

$$r_\infty = 0.99575 - 0.09069\rho + 1.227\rho^2, \qquad (20)$$

except that the last coefficient is 1.227 in [40] as opposed to 1.1227 in [45]. We believe this is a typographical error, given that in the same book [40] (pp. 1–15) they show the Clausius-Mossotti equation

$$\mathscr{R}_{CM} = 0.99575 - 0.09069\rho + 1.1227\rho^2, \qquad (21)$$

which is the same as Eq. (19).

Younglove [41] derived a density-, temperature-, and pressure-dependent Clausius-Mossotti relationship

$$\mathscr{R}_{CM} = A + B\rho + C\rho^2 + D\rho^3 + ET + FP, \qquad (22)$$

with densities in mol/dm^3 and the following coefficients: $A = 0.20245443 \times 10^{-2}$, $B = 0.37171832 \times 10^{-6}$, $C = -0.92085013 \times 10^{-8}$, $D = -0.34065329 \times 10^{-11}$, $E = 0$, and $F = 0$ (see pp. 1–349 in [41]). Since in most formulas of specific refraction the density is in g/cm^3 instead of mol/dm^3 as in [41], Cauchy's coefficients for wavelength correction in Eq. (13) must be multiplied by the molar mass/1000. For H_2, the molar weight is 2.01594 g/mol [41].

2. Temperature dependence of the refractive index

Usually, the temperature dependence of the refractive index is not given explicitly, but rather implicitly through the temperature dependence of the density. We only found one explicit temperature-dependent formula of refractive index by McCarty [42] and many other explicit formulas for the temperature dependence of density (see, for example, [37,42]).

McCarty [42] used a modified Benedict-Webb-Rubin equation of state for para-H_2 which considers the temperature dependence of density and expands specific refraction into a power series to get a formula for the temperature dependence of the refractive index (see p. 7 of [42])

$$n = 1.0509586594 + 0.091463402563\epsilon^{0.41043983753}.$$
$$(23)$$

This formula assumed that $T_c = 32.93313976$ K, although not all digits are significant as McCarty gives $T_c = 32.933$ K elsewhere in the same work. A hint that not all digits are significant in Eq. (23) is the fact that the temperature-dependent density parameters are given, for example, as $A1 = -1.0880215243 \pm 0.214$ (see p. 3 in [42]). This suggests that the error on $A1$ propagated also to the refractive index and not all digits in Eq. (23) are significant. Equation (23) could also be corrected for wavelength with Eq. (14).

Jungwoon's review of p-H_2 data gave the following corrections for temperature-dependent density [37]:

$$\rho_{liquid} = \rho_c[1 + 1.7707(1 - \epsilon)^{0.3817}],$$
$$\rho_{gas} = \rho_c\{-0.01397 + 0.63032 \exp[-(1 - \epsilon)/0.16013]$$
$$+ 0.37572 \exp[-(1 - \epsilon)/0.01365]\}. \qquad (24)$$

The corrections given by Eqs. (23) and (24) could be substituted into any or all of Eqs. (18), (19), and (22) above to get a more accurate estimate of the refractive index at each temperature. Subsequently, turbidity fitting using Eq. (8)
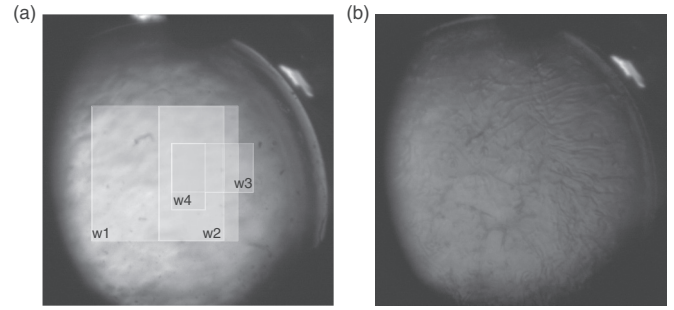

FIG. 4. Sample cell unit with H_2 at (a) $T = 35$ K and (b) $T = 33.008$ K. Four overlapping windows (marked w1–w4) were used for transmitted light intensity measurements. As the temperature approached $T_c = 33.0065$ K, less light was transmitted (b).

could be done with refractive indices corresponding to actually measured temperature instead of using only n_c for the entire temperature range. Additionally, correcting the specific refraction for both temperature with Eq. (23) and wavelength with Eq. (14) could improve the fitting of turbidity data.

C. Fitting turbidity data for hydrogen

In the following, we only show the fitting results for two refractive indices selected from Table III. A summary of some of our fitting results for H_2 is shown in Table IV for a constant index of refraction, i.e., for $n_c = 1.04911$ (measured at 546.2 nm) as listed in the first row of Table III. Since the wavelength at which the refractive index was measured is given, we use Eq. (17) to correct the refractive index for the wavelengths of our particular filters. The procedure is similar for any other constant refractive index from Table III.

The second example uses one of the most complex refractive index formulas we found in the literature and includes the temperature dependence of the refractive index as shown in Eq. (23) (see p. 7 of [42]). The results for the temperature-dependent refractive index (23) are summarized in Table V. Given the complexity of the formula, we performed the following different fittings shown in Table V from Ref. [42]: (i) $n_c = 1.0509586594 = $ const; (ii) $n_c = 1.0509586594 = $ const, corrected with Eq. (17) for the wavelengths of our filters (since no wavelength was provided, we assumed that $\lambda \to \infty$, i.e., assumed that n_c was derived from dielectric constant measurements); (iii) use the above filter-corrected values for n_c and further add the temperature dependence from Eq. (23); and (iv) use the temperature dependence from Eq. (23) with no wavelength correction.

We fitted the turbidity data for each of the three colors (red, 669.4 nm; green, 519.4 nm; and blue, 465.2 nm) and for each of the four window locations shown in Fig. 4(a). Representative turbidity plots versus reduced temperature data are shown in Fig. 5 for all three color filters used in this experiment. The data far from T_c give the background turbidity $\tau \approx \tau_B$. The data closer to T_c, where a is still small and $F(a)$ nearly constant (approximately equal to 8/3), give the isothermal compressibility $\tau \propto \kappa_T \propto \epsilon^{-\gamma}$ [slope approximately equal to $-\gamma$ in Fig. 5(a)]. Close to the critical point and for $a \geqslant 1$, $F(a)$ compensates the divergence of κ_T and the turbidity exhibits a logarithmic behavior, thus allowing the determination of ξ

TABLE IV. Fitting results for a relatively small refractive index $n_c = 1.049\,11$ measured at 546.2 nm [38].

n_c	Color	$\kappa_{T0} \times 10^9$ (Pa^{-1})	ξ_0 (Å)	τ_B (m^{-1})	χ^2	R^2
1.04911	red	76.2 ± 4.3	1.57 ± 0.10	0.99 ± 0.14	0.251	0.992
(546.2 nm)	red	57.5 ± 0	1.12 ± 0.03	1.51 ± 0.13	0.447	0.986
	red	85.2 ± 1.4	1.78 ± 0	0.81 ± 0.12	0.281	0.991
	red	57.5 ± 0	1.78 ± 0	2.41 ± 0.33	3.674	0.887
	green	68.8 ± 5.5	2.77 ± 0.18	0.83 ± 0.19	0.332	0.991
	green	57.5 ± 0	1.20 ± 0.10	3.13 ± 0.35	3.44	0.905
	green	41.7 ± 1.1	1.78 ± 0	1.63 ± 0.22	0.837	0.977
	green	57.5 ± 0	1.78 ± 0	0 ± 0.42	6.143	0.831
	blue	69.3 ± 7.8	3.36 ± 0.28	0.54 ± 0.26	0.594	0.986
	blue	57.5 ± 0	2.92 ± 0.05	0.87 ± 0.18	0.637	0.985
	blue	32.09 ± 1.18	1.78 ± 0	1.83 ± 0.32	1.813	0.957
	blue	57.5 ± 0	1.78 ± 0	0 ± 1.03	36.428	0.129
1.04857	red	78.0 ± 4.4	1.57 ± 0.10	0.99 ± 0.14	0.251	0.992
from Eq. (17)	red	57.5 ± 0	1.09 ± 0.03	1.55 ± 0.13	0.483	0.985
	red	87.21 ± 1.42	1.78 ± 0	0.81 ± 0.12	0.281	0.991
	red	57.5 ± 0	1.78 ± 0	2.48 ± 0.34	4	0.877
1.04929	green	68.3 ± 5.5	2.77 ± 0.18	0.83 ± 0.19	0.332	0.991
from Eq. (17)	green	57.5 ± 0	2.41 ± 0.04	1.13 ± 0.13	0.382	0.99
	green	41.4 ± 1.1	1.78 ± 0	1.63 ± 0.22	0.836	0.977
	green	57.5 ± 0	1.78 ± 0	0 ± 0.44	6.488	0.821
1.04977	blue	67.4 ± 7.5	3.35 ± 0.28	0.54 ± 0.26	0.594	0.986
from Eq. (17)	blue	57.5 ± 0	2.98 ± 0.05	0.81 ± 0.18	0.62	0.985
	blue	31.2 ± 1.2	1.78 ± 0	1.83 ± 0.32	1.811	0.957
	blue	57.5 ± 0	1.78 ± 0	0 ± 1.11	41.736	0.002

[slope approximately equal to $-\nu$ in Fig. 5(b)]. Note that a leveling off of the turbidity near T_c can occur if the density is not strictly equal to the critical density. This question of density close to the critical value becomes very limiting when one approaches the critical temperature very closely [21]. This effect can be correctly analyzed only using the universal Ising-like parametric form of the fluid equation of state (see, for example, Refs. [48,49]). Such a complex analysis can be ignored for our present experimental approach of the critical point.

However, we note that when the density is off-critical, one observes a phase change at the coexistence temperature T_{cx} instead of T_c. As a result, the temperature scale then becomes $T/T_{cx} - 1$ instead of the reduced temperature $\epsilon = T/T_c - 1$. Furthermore, the turbidity divergence is replaced by turbidity saturation. For a detailed explanation of the reasons behind the estimated slopes in Fig. 5, see the numerical estimation of the power law exponents based on the theoretical formula of turbidity given by Eq. (8) in Sec. IV E.
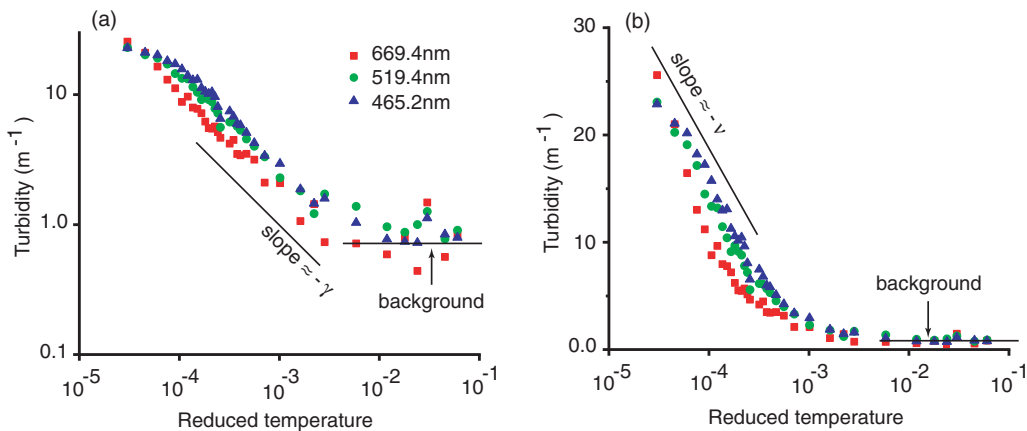

FIG. 5. Turbidity variation with reduced temperature in (a) log-log and (b) semilogarithmic scale for all three filters. The region far from T_c in (a) highlights the background contribution (horizontal line). Closer to T_c, the divergence of the isothermal compressibility leads to a straight fitting line with a slope approximately equal to $-\gamma$ in (a). The region very close to T_c in the log-linear plot of (b) reveals the contribution of the interference term from which the correlation length can be determined [straight line with slope approximately equal to $2\nu - \gamma \approx -\nu$ in (b)].

TABLE V. Fitting results for a temperature-dependent refractive index from Ref. [42]. The best fitting results are highlighted in bold for each index of refraction and filter color.

n_c	Color	$\kappa_{T0} \times 10^9$ (Pa^{-1})	ξ_0 (Å)	τ_B (m^{-1})	χ^2	R^2
1.0509586594 = const	red	70.4 ± 4.0	1.56 ± 0.10	0.99 ± 0.14	0.251	0.992
from Eq. (23) at T_c	red	57.5 ± 0	1.24 ± 0.03	1.36 ± 0.11	0.347	0.989
	green	63.6 ± 5.1	2.76 ± 0.18	0.83 ± 0.19	0.332	0.991
	green	57.5 ± 0	2.55 ± 0.04	1.00 ± 0.13	0.348	0.99
	blue	64.1 ± 7.2	3.35 ± 0.28	0.54 ± 0.26	0.594	0.986
	blue	57.5 ± 0	3.09 ± 0.05	0.72 ± 0.18	0.598	0.986
1.05208 = const	red	67.3 ± 3.8	1.56 ± 0.10	0.99 ± 0.14	0.251	0.992
from Eq. (17) at T_c	red	57.5 ± 0	1.31 ± 0.03	1.28 ± 0.11	0.305	0.99
1.05284 = const	green	$\mathbf{58.9 \pm 4.7}$	$\mathbf{2.76 \pm 0.18}$	$\mathbf{0.83 \pm 0.19}$	**0.332**	**0.991**
from Eq. (17) at T_c	green	57.5 ± 0	2.71 ± 0.04	0.87 ± 0.13	0.333	0.991
1.05332 = const	blue	$\mathbf{58.2 \pm 6.5}$	$\mathbf{3.34 \pm 0.28}$	$\mathbf{0.54 \pm 0.26}$	**0.594**	**0.986**
from Eq. (17) at T_c	blue	57.5 ± 0	3.31 ± 0.05	0.55 ± 0.18	0.579	0.986
1.05208	red	$\mathbf{59.6 \pm 3.1}$	$\mathbf{1.45 \pm 0.09}$	$\mathbf{0.94 \pm 0.14}$	**0.241**	**0.992**
from Eq. (17) with Eq. (23)	red	57.5 ± 0	1.39 ± 0.03	1.01 ± 0.09	0.237	0.993
1.05284	green	49.4 ± 3.7	2.49 ± 0.16	0.78 ± 0.19	0.335	0.991
from Eq. (17) with Eq. (23)	green	57.5 ± 0	2.82 ± 0.04	0.49 ± 0.14	0.382	0.99
1.05332	blue	47.4 ± 4.9	2.98 ± 0.24	0.47 ± 0.27	0.601	0.986
from Eq. (17) with Eq. (23)	blue	57.5 ± 0	3.44 ± 0.06	0.11 ± 0.19	0.656	0.985
1.050958	red	$\mathbf{62.2 \pm 3.3}$	$\mathbf{1.44 \pm 0.09}$	$\mathbf{0.94 \pm 0.14}$	**0.241**	**0.992**
with Eq. (23)	red	57.5 ± 0	1.32 ± 0.03	1.09 ± 0.10	0.251	0.992
	green	$\mathbf{53.0 \pm 4.0}$	$\mathbf{2.49 \pm 0.16}$	$\mathbf{0.78 \pm 0.19}$	**0.335**	**0.991**
	green	57.5 ± 0	2.66 ± 0.04	0.62 ± 0.13	0.35	0.99
	blue	$\mathbf{51.8 \pm 5.4}$	$\mathbf{2.97 \pm 0.24}$	$\mathbf{0.47 \pm 0.27}$	**0.602**	**0.986**
	blue	57.5 ± 0	3.21 ± 0.05	0.27 ± 0.18	0.608	0.986

For each refractive index in Tables IV and V, the fitting results are shown as the mean plus or minus standard deviation (s.d.). The mean value was computed over the four fitting values corresponding to each of the four windows shown in Fig. 4. The fitting was performed in four different ways (see Tables IV and Fig. 6): (i) κ_{T0}, ξ_0, and τ_B were all free parameters; (ii) $\kappa_{T0} = 57.5 \times 10^{-9}$ Pa^{-1} (± 0 s.d.), while both ξ_0 and τ_B were free parameters; (iii) $\xi_0 = 1.78$ Å (± 0 s.d.),

while both κ_{T0} and τ_B were free parameters; and (iv) $\kappa_{T0} = 57.5 \ 5 \times 10^{-9}$ Pa^{-1} (± 0 s.d.), $\xi_0 = 1.78$ Å (± 0 s.d.), and τ_B was a free parameter.

The reference values $\kappa_{T0} = 57.5 \times 10^{-9}$ Pa^{-1} and $\xi_0 = 1.78$ Å are predicted using the master crossover functions [50] for one-component fluids constructed from the mean crossover functions for uniaxial three-dimensional Ising-like systems calculated in [27,50]. Consequently, when the four
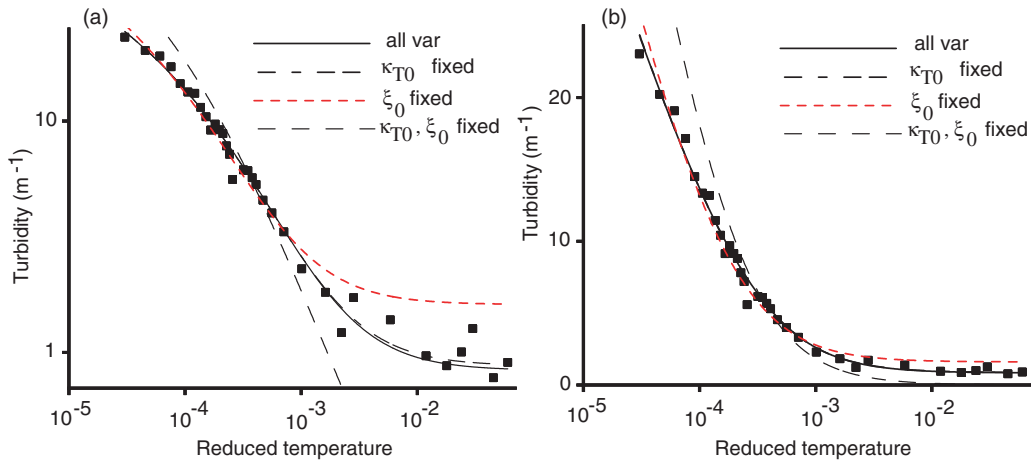

FIG. 6. (a) A log-log (a) and (b) a log-linear plot of experimental turbidity data (closed squares) and four different fitting conditions for a green filter with four windows with κ_{T0}, ξ_0, and τ_B free parameters (solid line); $\kappa_{T0} = 57.5 \times 10^{-9}$ Pa^{-1}, ξ_0, and τ_B free parameters (long-dash–short-dashed line); $\xi_0 = 1.78$ Å, κ_{T0}, and τ_B free parameters (short-dashed line); and $\kappa_{T0} = 57.5 \times 10^{-9}$ Pa^{-1}, $\xi_0 = 1.78$ Å, and τ_B free parameter (long-dashed line).

critical coordinates of the critical point of any one-component fluid are known, the leading amplitudes of any singular physical property related to its corresponding master crossover function can be directly estimated [see, for example, Eqs. (71) and (72) and the data of Table III from [50] for the above referenced values of concern]. These values are very close to the n-H$_2$ values $\kappa_{T0} = 57.56 \times 10^{-9}$ Pa^{-1} and $\xi_0 = 1.745$ Å as reported in [10], Table 1.6, p. 44. In the same table, the values for p-H$_2$ were unknown for κ_{T0} and $\xi_0 = 1.54$ Å [10].

The fitting results in Table IV for each refractive index and filter color follow the above order of fitting parameter constraints. For example, the first row of Table IV is for $n_c = 1.049\,11$ measured at 546.2 nm according to Ref. [38]. It contains a row for each of the three filters used in the experiment (red, green, and blue). For $n_c = 1.049\,11$ measured at 546.2 nm for the red filter, there are four different fitting averages depending on which parameters were constant during the fitting procedure. The first row has all free parameters and reads $\kappa_{T0} = (76.2 \pm 4.3) \times 10^{-9}$ Pa^{-1}, $\xi_0 = (1.57 \pm 0.10)$ Å, and $\tau_B = (0.99 \pm 0.14)$ m^{-1}. The goodness of fit is measured by $\chi^2 = 0.251$ (the smaller the better) and adjusted $R^2 = 0.992$ (the larger the better).

The next row in Table IV has an index of refraction $n_c = 1.048\,57$ from Eq. (17). This means that we used the experimentally measured index of refraction $n_c = 1.049\,11$ (at 546.2 nm) from the first row and Eq. (17) to correct for the corresponding wavelength of the filter used in our experiment (red, green, and blue).

Two of the four fitting averages for each case are obviously off due to very high χ^2 and small, sometimes even negative R^2. This can be clearly seen also from Fig. 6, where we show only one example, i.e., the green filter with window 4. The fitting with only $\xi_0 = 1.78$ Å fixed (short-dashed line) severely overestimates the background turbidity, whereas the fitting with both $\kappa_{T0} = 57.5 \times 10^{-9}$ Pa^{-1} and $\xi_0 = 1.78$ Å fixed (long-dashed line) does not even converge (see Fig. 6). The two fittings with either all three parameters κ_{T0}, ξ_0, and τ_B free (solid line) or only $\kappa_{T0} = 57.5 \times 10^{-9}$ Pa^{-1} fixed (long-dash–short-dashed line) are almost indistinguishable from each other, except for some minute differences at large temperature visible only on a log-log plot [Fig. 6(a)]. Therefore, we did not further consider the fittings with $\xi_0 = 1.78$ Å fixed and the fittings with $\kappa_{T0} = 57.5 \times 10^{-9}$ Pa^{-1} and $\xi_0 = 1.78$ Å fixed. The only reasonable fittings are the first two lines of each filter color, i.e., with all three parameters free or with $\kappa_{T0} = 57.5 \times 10^{-9}$ Pa^{-1} fixed in our analysis.

Since we never used the fitting results with ξ_0 fixed, i.e., the third line in each fitting result shown in Table IV, and with both κ_{T0} and ξ_0 fixed, i.e., the fourth line in each fitting result shown in Table IV, such fitting results are no longer shown for the temperature-dependent refractive index example in Table V. This was done in order to avoid showing an exceedingly large table of which we only use half of the fitting results for further analysis.

While Tables IV and V are comprehensive, we also presented the data in a condensed graphical form in Fig. 7. We notice that the three filters provided estimates that are clearly separated in nonoverlapping clusters. The red filter provides the closest estimate to the expected values of both
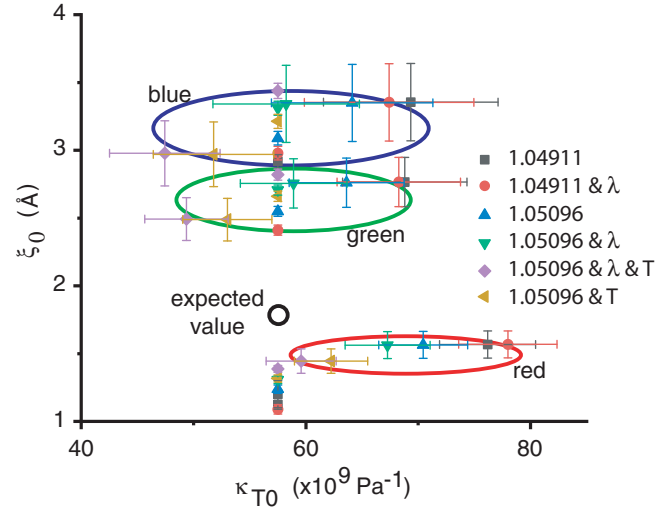

FIG. 7. Two representative refractive indices $n_c = 1.049\,11$ and $n_c = 1.050\,96$ with wavelength correction (marked by λ) and temperature-dependence (marked by T). There is a consistent increase of ξ_0 between red, green, and blue filters.

κ_{T0} and ξ_0: $\kappa_{T0} = (59.6 \pm 3.1)$ 10^{-9} Pa^{-1}, $\xi_0 = (1.45 \pm 0.09)$ Å, and $\tau_B = (0.94 \pm 0.14)$ m^{-1} for $n_c = 1.050\,958$ corrected for both filter color with Eq. (17) and temperature with Eq. (23). It seems however that the filter color correction of the refractive index is less important than the temperature correction as the next best parameter estimation is $\kappa_{T0} = (62.2 \pm 3.3) \times 10^{-9}$ Pa^{-1}, $\xi_0 = (1.44 \pm 0.09)$ Å, and $\tau_B = (0.94 \pm 0.14)$ m^{-1}.

For the green filter, $n_c = 1.050\,958$ corrected for filter color gives $\kappa_{T0} = (58.9 \pm 4.7) \times 10^{-9}$ Pa^{-1}, $\xi_0 = (2.76 \pm 0.18)$ Å, and $\tau_B = (0.83 \pm 0.19)$ m^{-1}. The next best fitting result is for $n_c = 1.050\,958$ corrected for temperature with Eq. (23), which gives $\kappa_{T0} = (53.0 \pm 4.0) \times 10^{-9}$ Pa^{-1}, $\xi_0 = (2.49 \pm 0.16)$ Å, and $\tau_B = (0.78 \pm 0.19)$ m^{-1}.

For the blue filter, $n_c = 1.050\,958$ corrected for filter color gives $\kappa_{T0} = (58.2 \pm 6.5) \times 10^{-9}$ Pa^{-1}, $\xi_0 = (3.34 \pm 0.28)$ Å, and $\tau_B = 0.54 \pm 0.26$ m^{-1}. The next best fitting result for this filter is for $n_c = 1.050\,958$ corrected for temperature with Eq. (23), which gives $\kappa_{T0} = (51.8 \pm 5.4) \times 10^{-9}$ Pa^{-1}, $\xi_0 = (2.97 \pm 0.24)$ Å, and $\tau_B = 0.47 \pm 0.27$ m^{-1}.

With all free parameters, we notice from Fig. 7 that the estimation of κ_{T0} comes within one standard deviation of the expected value $\kappa_{T0} = 57.5 \times 10^{-9}$ Pa^{-1} in the case of $n_c = 1.050\,958$. It is also clear from Tables IV and V that the estimated ξ_0 decreases with the filter's wavelength, while imposing a unique value of $\xi_0 = 1.78$ Å for all filters overestimates the κ_{T0} for the red filter and severely underestimates it for the green and blue filters. In addition, the estimated values of ξ_0 and τ_B are virtually the same whether all three parameters are free or if we impose $\kappa_{T0} = 57.5 \times 10^{-9}$ Pa^{-1}. In light of the above results, the fitting method gives consistent results across all filters.

Equation (11) gives an explicit formula for the sensitivity of turbidity (8) to small changes in refractive index and wavelength. To complete the sensitivity analysis of turbidity (8), we also checked how the fitting results change when the critical temperature $T_c = 33.0065$ K is shifted a few mK around the
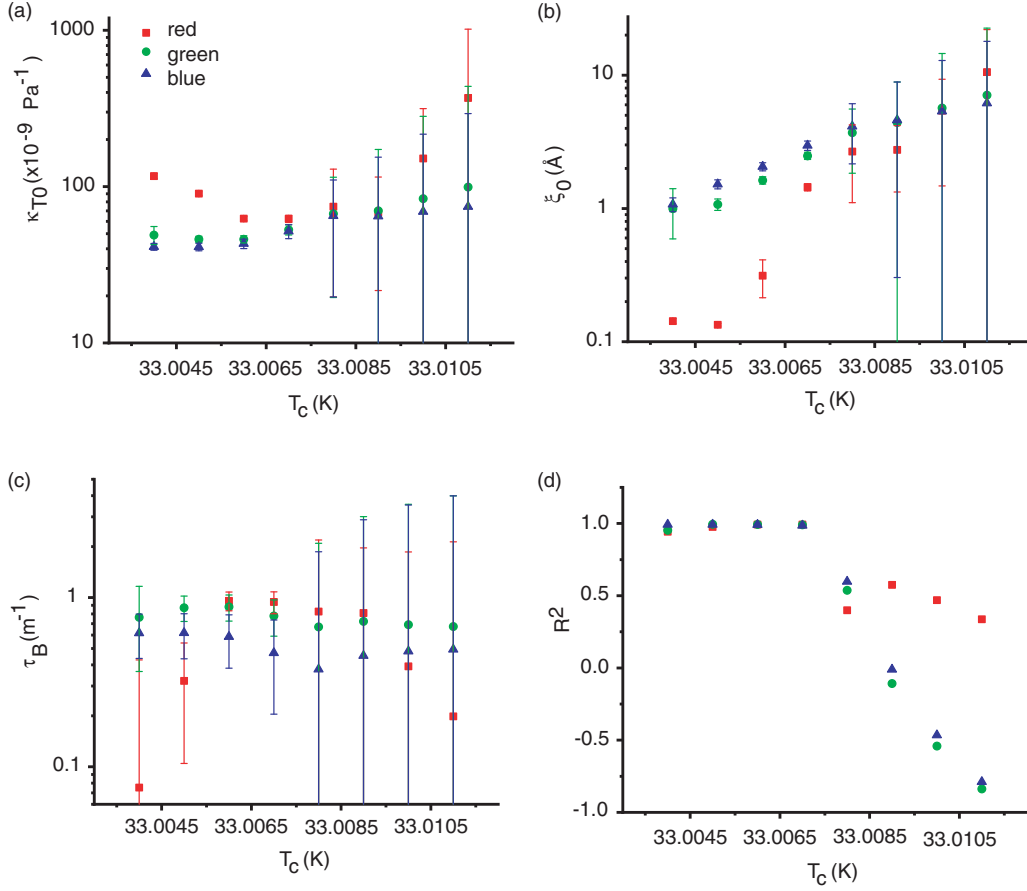
FIG. 8. Fitting parameters (a) κ_{T0}, (b) ξ_0, and (c) τ_B all change slightly by changing the value of T_c around the measured 33.0065 K. (d) The best fitting with the smallest error bars and the largest adjuster R^2 is for $T_c = 33.0065$ K.

measured value. Although we performed the analysis for all data, in Fig. 8 we only present the results for the last example from Table V.

We notice from Fig. 8 that by slightly shifting T_c below the measured value of 33.0065 K the error bars start rapidly increasing with the distance from $T_c = 33.0065$ K. However, the adjusted R^2 [Fig. 8(d)] remains reasonably high, which indicates an acceptable fit. For temperatures slightly larger than 33.0065 K, the fitting errors are very large and R^2 deteriorates quickly.

To conclude, for the index of refraction $n_c = 1.050\,958$ that was corrected for filter wavelength with Cauchy's formula given by Eq. (14), we found that (i) $\kappa_{T0} = (59.6 \pm 3.1) \times 10^{-9}$ Pa^{-1} and $\xi_0 = (1.45 \pm 0.09)$ Å for the red filter, (ii) $\kappa_{T0} = (58.9 \pm 4.7) \times 10^{-9}$ Pa^{-1} and $\xi_0 = (2.76 \pm 0.18)$ Å for the green filter, and (iii) $\kappa_{T0} = (58.2 \pm 6.5) \times 10^{-9}$ Pa^{-1} and $\xi_0 = (3.34 \pm 0.28)$ Å for the blue filter (see Table V for additional fitting results).

D. Comparison with existing data

One of the earliest experiments on liquid H$_2$ was performed by Johnston *et al.* [51]. They measured the pressure versus volume for seven isotherms with temperature between 20.38 and 32.58 K of normal liquid H$_2$. Even though the last isotherm at 32.58 K is not quite the critical temperature of n-H$_2$ of $T_c = 33.19$ K, it gives us a rough estimate of what should be the range of compressibility. We fitted their data

(not shown) and found that the compressibility reaches almost 80×10^{-9} Pa^{-1} at a pressure of 23.672 atm and temperature of 32.58 K. The extrapolation to $p_c = 12.89$ atm (see Table I) gives a compressibility in the range $(130–160) \times 10^{-9}$ Pa^{-1}. While isothermal compressibility diverges near T_c, these estimates give us a hint as to what to expect for the order of magnitude of the critical amplitude κ_{T0}.

Theoretical predictions based on the van der Waals model have four different asymptotic forms (see Table III in [52]).

(i) For $\epsilon > 0$ at ρ_c, the isothermal compressibility is given by $\kappa p_c = g\epsilon^{-\gamma}$, with $\gamma = 1$ (as opposed to $\gamma = 1.239$ from the three-dimensional Ising model) and $g = 1/6$. As a result, the estimated critical amplitude is $\kappa_{T0} = g/p_c \approx 127 \times 10^{-9}$ Pa^{-1}.

(ii) For $\epsilon < 0$ and along the p-V coexistence curves, the isothermal compressibility is given by $\kappa p_c = g'(-\epsilon)^{-\gamma'}$, with $\gamma' = 1$ and $g' = 1/12$. As a result, the estimated critical amplitude is $\kappa'_{T0} = g'/p_c \approx 63 \times 10^{-9}$ Pa^{-1}.

(iii) For $\epsilon > 0$ at P_c, the isothermal compressibility is given by $\kappa p_c = g_p\epsilon^{-\gamma}$, with $\gamma = 2/3$ and $g_p = 1/(3^{1/3} \times 6)$. As a result, the estimated critical amplitude is $\kappa_{T0}p = g_p/p_c \approx 88 \times 10^{-9}$ Pa^{-1}.

(iv) For $\epsilon < 0$ at P_c, the isothermal compressibility is given by $\kappa p_c = g'_p(-\epsilon)^{-\gamma'}$, with $\gamma' = 2/3$ and $g'_p = 1/(3^{1/3} \times 6)$. As a result, the estimated critical amplitude is $\kappa_{T0}p' = g'_p/p_c \approx 88 \times 10^{-9}$ Pa^{-1}.

For a somewhat different theoretical perspective, Ivanov [53] summarized a large body of data and found a strong correlation between critical exponents and critical amplitudes. The isothermal compressibility is given by its usual formula [see Eq. (2) in [53]]

$$p_c \kappa_T = \Gamma \epsilon^{-\gamma}.$$

Based on Eq. (19), different critical point studies ranging from the three-dimensional Ising model to theoretical models of CO_2 to experiments with Xe, NH_3, and SF_6 concluded that the correlation between the amplitude Γ and the critical exponent is [see Eq. (4) in [53]]

$$\Gamma \gamma^g = \gamma_0,$$

with $g = 7.15 \pm 0.16$ and $\gamma_0 = 0.23 \pm 0.01$. Based on [53], the critical amplitude $\kappa_0 = \frac{\Gamma}{p_c} = \frac{\gamma_0}{\gamma^g p_c} = 37.789 \times 10^{-9}$ Pa^{-1}, where we used $\gamma = 1.239$ and $p_c = 1.315$ MPa (see Table I). Even if we assume that the values of γ and p_c are exact, the propagated relative error on κ_0 is $\frac{\delta \gamma_0}{\gamma_0} + \ln(\gamma)\delta g \approx 7.8\%$, i.e., $\kappa_0 = (37.8 \pm 2.9) \times 10^{-9}$ Pa^{-1}. One of the main points of the study is that the critical amplitudes and critical coefficients vary widely from study to study even for the same substance. In addition, the study did not include any data for critical H_2. Therefore, this estimation of critical amplitude κ_0 for H_2 could be less than optimal.

To summarize, reasonable agreement was found with the expected compressibility [$\kappa_{T0} = 57.56 \times 10^{-9}$ Pa^{-1} (see Table 1.6 on p. 44 in [10]) and $\kappa_{T0} = 57.5 \times 10^{-9}$ Pa^{-1} (in [50])], while a correlation length is found larger than the expected values of $\xi_0 = 1.745$ Å (see Table 1.6 on p. 44 in [10]) and $\xi_0 = 1.78$ Å (in [50]). The most likely reason is that the correlation length determination needs data very close to T_c where even small off-criticality in density can cause large changes in turbidity.

E. Estimates of power law exponents

As we previously mentioned, the interference function $F(a)$ in Eq. (9), for a reasonable range of 1 Å $\leqslant \xi_0 \leqslant 3$ Å and all wavelengths in the visible spectrum, is at least at 77.7% of its limit value of 8/3 for all $\epsilon > 10^{-3}$. In other words, for $\epsilon > 10^{-3}$ the interference function is quasiconstant and its effect on turbidity formula can be neglected. This approximation corresponds in H_2 to an off-critical temperature of about $T - T_c > 33$ mK. In other words, for $T - T_c > 33$ mK the temperature-dependent part of the turbidity formula given by Eq. (8) becomes

$$\tau \approx A \pi T_c (1 + \epsilon)\kappa_0 \epsilon^{-\gamma}(1 + a_\chi \epsilon^\Delta)8/3 \propto \epsilon^{-\gamma},$$

where the nonanalytical amplitude a_χ from Eq. (1) was used with $\Delta = 0.5$. Since in this study the temperature range is $\epsilon \in (10^{-5}, 10^{-2})$, no further corrections are needed. As a result, a plot of turbidity τ versus the reduced temperature ϵ should look like a power law with an exponent close to the value of $-\gamma$. However, the contribution of background turbidity τ_B becomes significant at large temperatures and may cover the above-mentioned power law trend. Therefore, there are two competing factors: (i) We need a wide range of large temperatures to get a good power law fit and (ii) as the temperature

departs from T_c towards larger temperatures the temperature-dependent turbidity $(1 + \epsilon)(1 + a_\chi \epsilon^\Delta)\epsilon^{-\gamma}$ becomes smaller than the background turbidity τ_B. As a result, depending on the level of background turbidity, the temperature range where one can determine the critical exponent γ is quite narrow. This may lead to significant errors in the estimation of γ from the power law fit of turbidity τ versus reduced temperature ϵ for large temperatures.

At the other extreme, we are interested in finding the asymptotic behavior of the turbidity formula given by Eq. (8) for very small values of the reduced temperature ϵ. Due to the asymptotic behavior of the correlation length $\xi = \xi_0 \epsilon^{-\nu}$, the variable a in the interference term $F(a)$ of Eq. (9) is asymptotically described by $a = 2(k_0 \xi)^2 \propto \epsilon^{-2\nu}$. As the reduced temperature decreases ($\epsilon \to 0$), the variable a diverges ($a \to \infty$). While the second term of $F(a)$ vanishes as $a \to \infty$, the first term leads to an ∞/∞ case, which can be solved with l'Hôpital's theorem and gives $\lim_{a \to \infty} F(a) = 0$. After minor rearrangements of some terms, it can be shown that the power series approximation of $F(a)$ for the case when a is very large, i.e., $\epsilon \to 0$, becomes

$$\frac{2 \ln(2)}{a} + \frac{2 \ln(2)}{a^2} + O(a^{-3}).$$

Therefore, the asymptotic behavior of $F(a)$ as $a \to \infty$ is $F(a) \approx \frac{2 \ln(2)}{a} \propto \epsilon^{2\nu}$. As a result, the temperature-dependent part of turbidity equation (8) becomes $\tau = A \pi T_c (1 + \epsilon)\kappa_0 \epsilon^{-\gamma} \frac{2 \ln(2)}{2(k_0 \xi_0 \epsilon^{-\nu})^2} \propto \epsilon^{2\nu - \gamma}$.

The exponents γ and ν are related by $\eta = 2 - \frac{\gamma}{\nu} \approx 0.02$ [54,55]. The Fisher exponent η, however, corresponds to an asymptotic correlation function different from Ornstein-Zernike theory and Eq. (8) is no longer valid. Since our data are not close enough to the critical point in terms of density and temperature, we will not discuss this issue further.

The above detailed analysis is confirmed by the plot of the apparent power law exponent ($\tau \propto \epsilon^x$) shown in Fig. 9(a), which was obtained from numerical simulation of the theoretical formula of turbidity given by Eq. (8). We notice that the absolute value of the apparent power law exponent x for large temperatures is smaller than γ. As we notice from Fig. 9(a), it is impossible to establish in what temperature range the power law exponent is in any way related to γ and/or ν. To gain some insight into the effect of the critical exponents γ and ν on the power law exponent of the theoretical turbidity formula given by Eq. (8), we carried out two sets of numerical simulations: with fixed $\gamma = 1.239$ and variable $\nu \in \{0.5, 0.6, 0.7\}$ [see solid lines in Figs. 9(b)–9(d)] and with fixed $\nu = 0.63$ and variable $\gamma \in \{1.1, 1.2, 1.3\}$ [see dotted lines in Figs. 9(b)–9(d)]. We notice that critical exponent ν only changes the apparent power law exponent of turbidity versus reduced temperature for small temperatures [see Fig. 9(b)]. Indeed, all three curves for $\nu \in \{0.5, 0.6, 0.7\}$ converge quite rapidly to the same trace and are indistinguishable for $\epsilon \geqslant 0.01$ [see Fig. 9(c)]. At the same time, γ covers a broad range of temperatures by shifting all power law exponents proportional to the value of γ. This trend is visible in all Figs. 9(b)–9(d) and the proportional shift covers $\epsilon \geqslant 5 \times 10^{-4}$.

To conclude, for reduced temperatures larger than $\epsilon \geqslant 5 \times 10^{-4}$, the apparent turbidity power law exponent is entirely
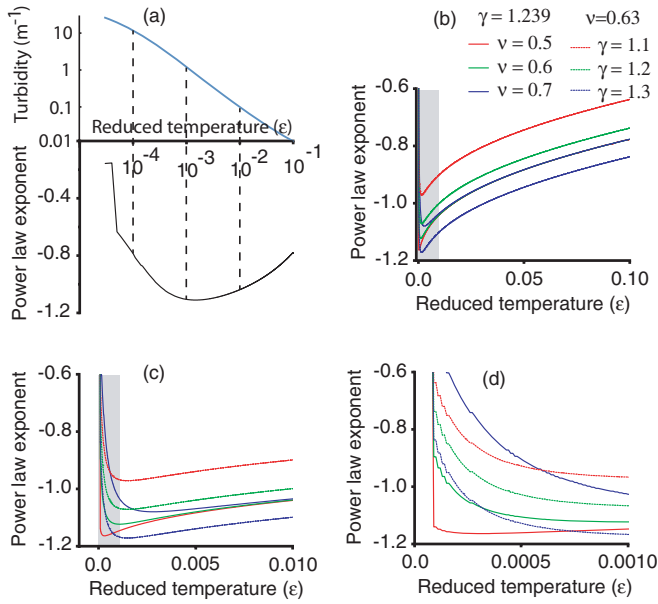
FIG. 9. Theoretical turbidity τ and its corresponding apparent power law exponent x ($\tau \propto \epsilon^x$). (a) The log-log plot of the theoretical turbidity formula given by Eq. (8) (top) and the corresponding apparent power law exponent x (bottom). The critical exponents were $\gamma = 1.239$ and $\nu = 0.63$. The reduced temperature range in our experiment was $\epsilon \in (10^{-5}, 10^{-2})$. (b) For a fixed $\gamma = 1.239$ a slight change of ν only affects the power law exponent at low temperatures. For $\epsilon \leqslant 5 \times 10^{-3}$ and $\nu = 0.5$ (red solid line), $\nu = 0.6$ (green solid line), and $\nu = 0.7$ (blue solid line), the power law exponent is very sensitive to ν. This is highlighted by the magnification of the shaded area of (b), which is shown in (c), and by further magnifying the shaded are in (c), which is shown in (d). For fixed $\nu = 0.63$, an increase in γ, i.e., $\gamma = 1.1$ (red dotted line), $\gamma = 1.2$ (green dotted line), and $\gamma = 1.3$ (blue dotted line) in panels (b)–(d), shows that the power law exponent is most sensitive to γ in the range $\epsilon \geqslant 5 \times 10^{-4}$.

determined by critical exponent γ. For reduced temperature $\epsilon \leqslant 5 \times 10^{-3}$, the critical exponent ν has a significant contribution to the apparent power law exponent.

V. CONCLUSION

Experiments near the critical point of cryogenic fluids like H_2 require suppressing gravity effects and pose a series of challenges. First, for safety reasons, it is almost impossible to perform such experiments in microgravity. This is the reason why the only feasible alternative is the use of magnetic compensation to simulate weightlessness. Second, careful consideration must be given to the experimental conditions such that the n-H_2 to p-H_2 ratio is correctly determined. Thermophysical properties are sensitive to the n-H_2 to p-H_2 ratio. Given that the relaxation time constant for H_2 is about 2500 min to reach the ortho-para equilibrium [34] and that experiments are performed within a couple of hours after filling in the cell, the sample cell contains mostly n-H_2. Finally, since turbidity is measured through light transmission measurements, careful consideration was given to the light source and its intensity so that we minimize the effect of light-induced heating of the sample cell.

The paper's main results are concerned with (i) the careful design of HYLDE to generate good quality data very near T_c through magnetic compensation of gravity, (ii) the use of image analysis for turbidity measurements corresponding to three different wavelengths centered on red, green, and blue filters, (iii) agreement of isothermal compressibility critical amplitude κ_{T0} with previous estimates, and (iv) better correlation length critical amplitude ξ_0 being obtained with data very near T_c and density closer to critical value.

This study shows that light transmission measurements directly on the image of a critical fluid sample can give turbidity data with comparable precision as the traditional techniques using a laser beam. Using different wavelength filters gives more useful data and allows us to cross-check the critical amplitude values. This technique shows great promise as it allows both a detailed observation of the sample and local measurement of turbidity. When a density gradients exist, as is often the case in space or magnetic weightlessness experiments, different regions of interest of those images can be selected and compared. The more turbid regions correspond to fluid density closest to the critical density.

Concerning H_2 under magnetic weightlessness, the data are fitted to the simplest formula (8) with isothermal compressibility, correlation length, and background turbidity as free parameters. One can see the extreme sensitivity of the fit to the refractive index value. Data the furthest from T_c provide the background turbidity estimate and compressibility terms, while data close to T_c give the correlation length. To summarize our results, for $n_c = 1.050\,958$ corrected for the filter wavelength we found (i) $\kappa_{T0} = (59.6 \pm 3.1) \times 10^{-9}$ Pa^{-1} and $\xi_0 = (1.45 \pm 0.09)$ Å for the red filter, (ii) $\kappa_{T0} = (58.9 \pm 4.7) \times 10^{-9}$ Pa^{-1} and $\xi_0 = (2.76 \pm 0.18)$ Å for the green filter, and (iii) $\kappa_{T0} = (58.2 \pm 6.5) \times 10^{-9}$ Pa^{-1} and $\xi_0 = (3.34 \pm 0.28)$ Å for the blue filter (the uncertainty is one standard deviation in Table V). These fitting results are in good agreement with previously published values for n-H_2 susceptibility: $\kappa_{T0} = 57.56 \times 10^{-9}$ Pa^{-1} (see Table 1.6 on p. 44 in [10]) and $\kappa_{T0} = 57.5 \times 10^{-9}$ Pa^{-1} (in [50]). In contrast, the correlation length was found larger than the expected value of $\xi_0 = 1.745$ Å (see Table 1.6 on p. 44 in [10]) and $\xi_0 = 1.78$ Å (in [50]). This discrepancy is due to the fact that data very near T_c are affected by even minute density deviations from critical density.

A more accurate estimation of critical amplitudes could be achieved by controlling the density gradient throughout the sample to ensure that critical density is truly reached at some places. For that purpose, a dedicated sample could be placed either slightly off the axis at the compensation point height or on the axis of the compensation point.

The present experimental method, which uses image analysis at different wavelengths for a fluid under reduced gravity by magnetic means, offers several benefits to the study of critical point phenomena. First, magnetic compensation of gravity allows a very close approach to the critical temperature without gravity disturbances that usually affect critical fluids, e.g., buoyancy-driven instabilities and strong density gradients. Second, the light intensity can be made very weak to negligibly disturb the temperature of the sample, which is extremely important for cryogenic fluids. Third, each image covers the whole sample, which allows us to detect density

inhomogeneities. In the case of imposed density gradients, the image analysis allows us to quantify the gradient. Fourth, other processes, such as phase transition, can be studied with the same setup. The critical temperature can thus be determined with high precision. Additionally, it is easy to vary turbidity intensities and cross-check results by using filters with different wavelengths.

ACKNOWLEDGMENTS

[1] T. Andrews, Philos. Trans. R. Soc. London **159**, 575 (1869).

[2] J. Rowlinson, Nature (London) **244**, 414 (1973).

[3] A. Lytle and D. Jacobs, J. Chem. Phys. **120**, 5709 (2004).

[4] D. Beysens, in *Materials Sciences in Space: A Contribution to the Scientific Basis of Space Processing*, edited by B. Feuerbacher, H. Hamacher, and R. J. Naumann (Springer, Berlin, 1986), p. 191.

[5] D. Chandler and I. Oppenheim, J. Chem. Phys. **49**, 2121 (1968).

[6] *Phase Transitions and Critical Phenomena*, edited by C. Domb and J. L. Lebowitz (Academic, New York, 2000), Vol. 18.

[7] A. Onuki, *Phase Transition Dynamics* (Cambridge University Press, Cambridge, 2002).

[8] V. Privman, P. Hohenberg, and A. Aharony, in *Phase Transitions and Critical Phenomena*, edited by C. Domb and J. L. Lebowitz (Academic, San Diego, 1991), Vol. 14.

[9] H. Stanley, *Introduction to Phase Transitions and Critical Phenomena* (Oxford University Press, Oxford, 1987).

[10] B. Zappoli, D. Beysens, and Y. Garrabos, *Heat Transfers and Related Effects in Supercritical Fluids* (Springer, Berlin, 2015).

[11] D. Chato, in *Proceedings of the 45th AIAA Aerospace Sciences Meeting and Exhibit, Reno, 2007* (American Institute of Aeronautics and Astronautics, Reston, 2005), paper 2007-953, pp. 1–10.

[12] S. Mustafi, E. Canavan, W. Johnson, B. Kutter, and J. Shull, in *Proceedings of the AIAA SPACE 2009 Conference and Exposition, Pasadena, 2009* (American Institute of Aeronautics and Astronautics, Reston, 2009), paper 2009-6584, pp. 1–10.

[13] C.-X. Wang, S.-H. Xu, Z.-W. Sun, and W.-R. Hu, Int. J. Heat Mass Transf. **53**, 1801 (2010).

[14] D. Chatain, D. Beysens, K. Madet, V. Nikolayev, and A. Mailfert, Microgravity Sci. Technol. **18**, 196 (2006).

[15] V. Nikolayev, D. Chatain, D. Beysens, and G. Pichavant, Microgravity Sci. Technol. **23**, 113 (2011).

[16] R. Wunenburger, D. Chatain, Y. Garrabos, and D. Beysens, Phys. Rev. E **62**, 469 (2000).

[17] L. Quettier, H. Felice, A. Mailfert, D. Chatain, and D. Beysens, Eur. Phys. J. Appl. Phys. **32**, 167 (2005).

[18] D. Chatain and V. Nikolayev, Cryogenics **42**, 253 (2002).

[19] V. G. Puglielli and N. C. Ford, Phys. Rev. Lett. **25**, 143 (1970).

[20] C. Lecoutre, Y. Garrabos, E. Georgin, F. Palencia, and D. Beysens, Int. J. Thermophys. **30**, 810 (2009).

[21] C. Lecoutre, R. Guillaument, S. Marre, D. Beysens, Y. Garrabos, and I. Hahn, Phys. Rev. E **91**, 060101(R) (2015).

[22] L. S. Ornstein and F. Zernike, in *17th Proceedings of the Royal Netherlands Academy of Arts and Sciences (KNAW)* (Elsevier, 1914), pp. 793–806.

[23] L. Ornstein and F. Zernike, Phys. Z. **19**, 134 (1918).

[24] D. Beysens and Y. Garrabos, Physica A **281**, 361 (2000).

[25] J. Zinn-Justin, *Quantum Field Theory and Critical Phenomena* (Clarendon, Oxford, 2002).

[26] C. Bagnuls and C. Bervillier, Phys. Rev. E **65**, 066132 (2002).

[27] Y. Garrabos and C. Bervillier, Phys. Rev. E **74**, 021113 (2006).

[28] Y. Garrabos, C. Lecoutre, S. Marre, R. Guillaument, D. Beysens, and I. Hahn, J. Stat. Phys. **158**, 1379 (2015).

[29] D. T. Jacobs, S. M. Y. Lau, A. Mukherjee, and C. A. Williams, Int. J. Thermophys. **20**, 877 (1999).

[30] A. Oprisan, J. J. Hegseth, G. M. Smith, C. Lecoutre, Y. Garrabos, and D. A. Beysens, Phys. Rev. E **84**, 021202 (2011).

[31] G. Gandikota, D. Chatain, T. Lyubimova, and D. Beysens, Phys. Rev. E **89**, 063003 (2014).

[32] T. Lyubimova, A. Ivantsov, Y. Garrabos, C. Lecoutre, G. Gandikota, and D. Beysens, Phys. Rev. E **95**, 013105 (2017).

[33] C. Air Liquide and S. Division, *Encyclopedie des Gaz* (Elsevier, Amsterdam, 1976), p. 9.

[34] T. Charignon, P. Lloveras, D. Chatain, L. Truskinovsky, E. Vives, D. Beysens, and V. S. Nikolayev, Phys. Rev. E **91**, 053007 (2015).

[35] H. Woolley, R. Scott, and F. Brickwedde, J. Res. Natl. Bur. Stand. **41**, 379 (1948).

[36] H. M. Roder, G. E. Childs, R. D. McCarty, and P. E. Angerhofer, *Survey of the Properties of the Hydrogen Isotopes below their Critical Temperatures*, National Bureau of Standards (US) Technical Note 641 (US GPO, Washington, DC, 1973).

[37] C. Jungwoon, Liquid hydrogen properties, HANARO Report No. KAERI/TR-2723/2004, Korea Atomic Energy Research Institute, 2004 (unpublished).

[38] P. C. Souers, Cryogenic hydrogen data pertinent to magnetic fusion energy, Report No. UCRL-52628, Lawrence Livermore Laboratory, 1979 (unpublished).

[39] H. M. Roder, L. A. Weber, and R. D. Goodwin, *Thermodynamic and Related Properties of Parahydrogen from the Triple Point to 100 K at Pressures to 340 Atmospheres*, National Bureau of Standards (US) Monograph 94 (US GPO, Washington, DC, 1965).

[40] R. D. McCarty, J. Hord, and H. M. Roder, *Selected Properties of Hydrogen*, National Bureau of Standards (US) Monograph 168 (US GPO, Washington, DC, 1981).

[41] B. A. Younglove, J. Phys. Chem. Ref. Data **11**, 1 (1982).

[42] R. D. McCarty, A modified Benedict-Webb-Rubin equation of state for parahydrogen, National Bureau of Standards Report No. NBSIR 74-357, 1974 (unpublished).

[43] H. Hoge and J. Lassiter, J. Res. Natl. Bur. Stand. **47**, 75 (1951).

[44] J. Stewart, J. Chem. Phys. **40**, 3297 (1964).

[45] R. J. Corruccini, *Refractive Index and Dispersion of Liquid Hydrogen*, NBS Technical Notes 323 (US GPO, Washington, DC, 1965).

[46] J. Koch, Ark. Mat. Astron. Fys. **8** (20) (1912).

[47] M. Kirn, Ann. Phys. (Leipzig) **64**, 566 (1921).

[48] Y. Garrabos, C. Lecoutre, S. Marre, and B. LeNeindre, J. Stat. Phys. **164**, 575 (2016).

[49] Y. Garrabos, C. Lecoutre, S. Marre, B. LeNeindre, and I. Hahn, J. Stat. Phys. **165**, 471 (2016).

[50] Y. Garrabos, C. Lecoutre, F. Palencia, B. Le Neindre, and C. Erkey, Phys. Rev. E **77**, 021116 (2008).

[51] H. L. Johnston, W. E. Keller, and A. S. Friedman, J. Am. Chem. Soc. **76**, 1482 (1954).

[52] D. C. Johnston, *Advances in Thermodynamics of the van der Waals Fluid* (Morgan and Claypool, San Rafael, 2014), pp. 2053–2571.

[53] D. Y. Ivanov, Dokl. Phys. **52**, 380 (2007).

[54] M. E. Fisher, Rep. Prog. Phys. **30**, 615 (1967).

[55] R. Kenna and B. Berche, Europhys. Lett. **105**, 26005 (2014).